Continuum and atomistic modeling of interacting graphene layers

J. Patrick Wilber,* Curtis B. Clemons, and Gerald W. Young
Department of Theoretical and Applied Mathematics, University of Akron, Akron, Ohio 44325-4002, USA

Alper Buldum
Department of Physics, University of Akron, Akron, Ohio 44325-4002, USA

D. Dane Quinn
Department of Mechanical Engineering, University of Akron, Akron, Ohio 44325-4002, USA
(Received 30 May 2006; revised manuscript received 26 September 2006; published 16 January 2007)

To investigate multishell models of multiwalled carbon nanotubes, we consider the buckling of a pair of graphene layers interacting by van der Waals forces. The layers are modeled as continuum sheets whose interaction is determined by a Lennard-Jones interatomic potential. Important in our treatment is the effect of nonequilibrium spacing between the layers, an issue whose physical and technological importance is suggested by a number of recent articles [see in particular, J. Zou *et al.*, Nano Lett. **6**, 430 (2006), and the references therein]. Using standard local bifurcation techniques, we construct bifurcation curves that describe the deformation of the layers as the edges of the layers are compressed. The bifurcation curves agree qualitatively with the sequence of deformations predicted by atomistic simulations. This agreement suggests the validity of multishell continuum models of multiwalled carbon nanotubes.

DOI: 10.1103/PhysRevB.75.045418 PACS number(s): 62.25.+g, 61.48.+c

I. INTRODUCTION

Carbon nanotubes have remarkable mechanical properties, most notably an extraordinary tensile strength combined with the flexibility to sustain large compressive loads and bending deformations elastically.[1–3] These properties naturally suggest certain applications, for example, using nanotubes as reinforcing fibers in composite materials or as probes in atomic force microscopy. Such applications have in turn motivated many investigations of how carbon nanotubes deform and buckle under axial loads.

Axial buckling problems have been studied for both single-walled and multiwalled nanotubes. Such problems for single-walled nanotubes are more readily described because of the relatively simple structure of a single-walled tube. Basic to this structure is graphene, a two-dimensional array or sheet of carbon atoms in a periodic hexagonal arrangement. A single-walled carbon nanotube can be visualized as a rectangular section cut from a larger graphene sheet and wrapped into the shape of a hollow cylinder. One of the first papers to treat the axial buckling of single-walled nanotubes is Ref. 4, in which the authors use molecular dynamics (MD) simulations to address two questions: what is the basic shape of an axially buckled single-walled nanotube, and can this buckling be accurately described by modeling the nanotube as a continuum. The authors conclude that linearly elastic shell theory can qualitatively predict the deformations observed in their MD simulation as well as the critical axial strains at which buckling occurs.

Other work on the axial buckling of a single-walled nanotube includes Refs. 5 and 6. These papers, similar in spirit to Ref. 4, contain the use of MD simulations or experiments to determine the basic geometry of compressively loaded nanotubes as a function of the length, diameter, and thickness of the tube. In particular, atomistic studies predict that under compressive loading, a nanotube with small aspect ratio buckles like a thin shell, a nanotube with an aspect ratio above a certain threshold buckles like a rod, and a nanotube with a very large aspect ratio undergoes a "wire-like" buckling with folding patterns similar to patterns observed in biomolecules such as DNA, RNA, and peptides. This interesting folding behavior has been explored in more detail in Ref. 7.

The treatment of axial buckling problems for multiwalled nanotubes is more challenging. A multiwalled nanotube is formed by nesting from two to as many as fifty single-walled nanotubes of different diameters along a common axis. The walls of adjacent tubes in a multiwalled nanotube are typically only a few angstroms apart. Consequently, adjacent walls interact through van der Waals forces, which are interatomic forces between pairs of nonbonded carbon atoms. Although these forces are much weaker than the forces between the covalently bonded neighboring carbon atoms within the wall of a given tube, van der Waals interactions appear to strongly influence the deformation of a multiwalled nanotube during axial compression and bending.

To explore the importance of van der Waals interactions for axial buckling, Ru in Ref. 8 proposed modeling each wall of a multiwalled nanotube as a thin linearly elastic shell. The equation for the radial displacement of each wall contains terms that describe the van der Waals forces between that wall and each of its nearest neighbors as a linear function of the relative radial displacement between the walls. By specializing these equations to a double-walled nanotube and using standard buckling analysis, Ru concludes in Ref. 8 that if the two tubes buckle in the same manner and if the two tubes are at their equilibrium spacing prior to buckling, then the critical axial strain at which buckling occurs for a double-walled tube is the same as the corresponding strain for just a single tube with the same elastic moduli. Ru[9,10] and Wang *et al.*[11,12] apply the same multishell model to explore the axial buckling of multiwalled nanotubes embedded in an elastic medium, or subject to external or internal pressure.

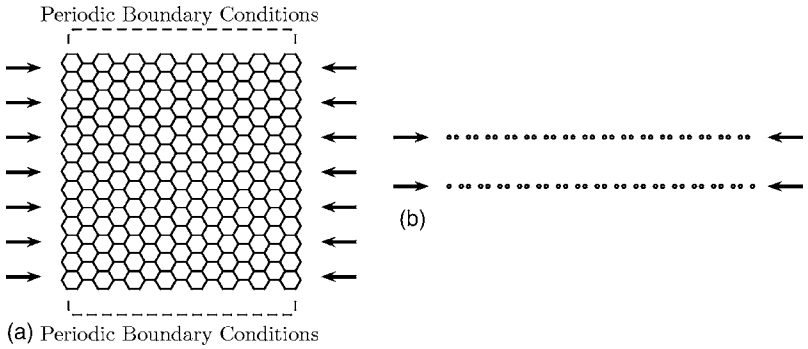

FIG. 1. Loading of interacting graphene layers. For each layer, a compressive load is applied along a pair of opposite edges. In the atomistic simulations, periodic boundary conditions are applied along the other edges. (a) View of the top layer from above. (b) Side view of the interacting layers.

For these various cases, the authors determine the critical axial buckling strain, compare this strain to the corresponding strain for a single-walled tube, and explore conditions under which it is accurate to model the multiwalled tube as a single thick-walled elastic tube.

In a related paper,[13] Ru explores similar questions using Euler-Bernoulli beam theory rather than linear shell theory to model a multiwalled nanotube as a collection of interacting beams. We note that the equations Ru uses in Ref. 13 are similar to those used in this paper, although, as seen below, the interpretation is different.

Recently, Han and Lu[14] modified Ru's multishell approach to treat torsional buckling, and Shen[15] used the multishell approach with a more sophisticated shell theory to treat the axial buckling and post-buckling behavior of multiwalled carbon nanotubes. Also, Refs. 16 and 17 treat multishell models in which the van der Waals interaction is permitted between all shells, not just nearest neighbors, and in which the van der Waals constants depend on the radii of the interacting cylindrical shells. Other recent work on buckling of multiwalled carbon nanotubes includes Refs. 18 and 19, in which questions about the relation between buckling patterns and aspect ratios are explored using a combination of atomistic simulations, continuum modeling, and finite element methods.

Little experimental work has focused explicitly on the effect of van der Waals interaction on the axial buckling of multiwalled nanotubes. However, recently Nishio *et al.*[20] presented a set of experiments in which a multiwalled nanotube is compressed between the tips of two probes of the type used in atomic force microscopy. Using this setup, the authors plot force versus displacement curves and, in particular, determine axial buckling loads. Then, using a novel experimental technique, Nishio *et al.*[20] remove the inner tubes of the multiwalled nanotube and repeat the axial buckling experiment on the remaining outer tubes. They thereby directly measure the effect of changing the number of walls. The authors report that the critical buckling force before and after the removal of the inner tubes are very close.

To explore the validity of the multishell modeling of multiwalled nanotubes, in this paper we consider the axial compression and buckling of a pair of parallel graphene layers that interact through a nonlinear van der Waals force. See Figs. 1 and 2. One can view these layers as small pieces excised from adjacent walls in a large multiwalled nanotube. As an alternative motivation, we note that recently developed techniques for isolating and manipulating individual graphene layers[21–24] and related theoretical work[25,26] suggest that graphene could become an important component in composite materials as well as in the design of nanoscale machines and devices. Hence there is a need to understand the mechanics of interacting graphene layers.

Because of its planar rather than cylindrical geometry, the formulation of this problem is simpler than that of the axial buckling for the full tube. We further simplify the problem by assuming that each of the two parallel graphene layers is infinitely wide and that the deformations are identical in each cross section perpendicular to the infinitely wide direction. Hence the transverse deflection of each cross section can be determined using the Euler-Bernoulli beam equation. Following Ru's approach, we model the van der Waals force by coupling the equations for each layer through a term that depends nonlinearly on the relative transverse displacements of the layers. The equilibrium equations are

$$\alpha u_1'''' - T u_1'' = f(u_1 - u_2 + d + \varepsilon a), \tag{1a}$$

$$\alpha u_2'''' - T u_2'' = -f(u_1 - u_2 + d + \varepsilon a), \tag{1b}$$

in which u_1, u_2 are the transverse displacements of the layer, α is the bending stiffness of each layer, T is the applied axial force per unit width, f is a nonlinear function describing the van der Waals force per unit area, ε is a small positive parameter, and a and d are constants the meanings of which are discussed shortly. Figures 1 and 2 depict the basic geometry of the problem. These equations are closely related to those studied in Ref. 13. However, Ru used the equations to model nested cylinders with a large aspect ratio and his work focuses mostly on the case $\varepsilon=0$. Here we model parallel layers and consider both $\varepsilon=0$ and $0<\varepsilon\ll 1$.

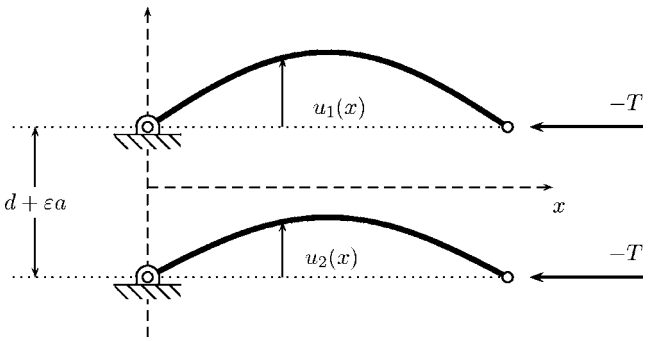

FIG. 2. Interacting graphene layers.

The system (1) is supplemented with classical "pinned-pinned" boundary conditions:

$$u_i(0) = u_i(l) = 0, \quad u_i''(0) = u_i''(l) = 0, \quad \text{for } i = 1,2, \tag{2}$$

in which l is the length of each layer.

We note that our formulation of the multishell model is more general than Ru's formulation (see references above) because we include a nonlinear expression for the van der Waals interaction between adjacent layers. Most of the ensuing analysis is local in nature and hence uses information only about $f'(d)$, which is equivalent to Ru's approach. However, to describe the branching solutions, we use the value of $f''(d)$; see (15), (18) below.

As noted above, we include the nonlinear terms on the right-hand side of (1) to describe the van der Waals interaction between the graphene layers. This interaction arises because, when the layers are sufficiently close, every carbon atom on, say, the bottom layer exerts a force on every carbon atom on the top layer. We let $f(\xi)$ denote the total van der Waals force per unit area exerted on a point on the top layer by all the atoms on the bottom layer when the point and the layer are a distance ξ apart. To find f, we assume the atoms are continuously distributed on the bottom layer with an atomic density σ and we assume the bottom layer is infinite in extent. (Hence this approach does not depend upon the exact placement of atoms on the two layers. See Ref. 27 for a discussion of this issue.) We then evaluate the improper integral

$$W(\xi) = \int_0^{2\pi} \int_0^{\infty} \sigma V(\sqrt{\xi^2 + r^2}) r dr d\theta, \tag{3}$$

where $V(s) := c_{12}s^{-12} - c_6 s^{-6}$ is the van der Waals energy between two nonbonded carbon atoms a distance s apart and $\sigma = 38.177$ nm^{-2}. The constants in V are

$$c_{12} = 3.859 \times 10^{-9} \text{ nN nm}^{13}, \quad c_6 = 2.43 \times 10^{-6} \text{ nN nm}^7 \tag{4}$$

(numerical values for c_6, c_{12}, and σ are taken from Ref. 28). It follows that

$$f(\xi) := -\sigma \frac{\partial W(\xi)}{\partial \xi} = 2\pi\sigma^2 \left(\frac{c_{12}}{\xi^{11}} - \frac{c_6}{\xi^5} \right). \tag{5}$$

The graph of f is depicted in Fig. 3. Note that f has a unique zero at $d = 0.341$ nm, which corresponds to the unique equilibrium spacing between the layers.

When considering the problem of compressive edge loading of interacting graphene layers, we wish to allow the spacing between the layers to deviate slightly from the equilibrium spacing d predicted by the van der Waals interaction. Recent research suggests that such deviations are likely to be important in the design and manufacture of nanoscale devices. See Ref. 29 and the references therein. To describe the spacing between the layers, we assume that the distance between the left edges of each layer and between the right edges of each layer is $d + \varepsilon a$, where $a = \pm 1$ and $0 \leqslant \varepsilon \ll 1$. See Fig. 2. Hence $d + \varepsilon a$ is a small deviation from the equilibrium spacing, with $a = 1$ corresponding to a spacing slightly greater than equilibrium and $a = -1$ corresponding to a spacing slightly less than equilibrium. For a point x on the top layer, $u_1(x) - u_2(x) + d + \varepsilon a$ is the vertical distance between the two layers at x. Therefore $f(u_1(x) - u_2(x) + d + \varepsilon a)$, the nonlinear term on the right-hand side of (1a), is the van der Waals force per unit area exerted on a point x on the top layer by the bottom layer. An analogous statement holds for the nonlinear term on the right-hand side of (1b).

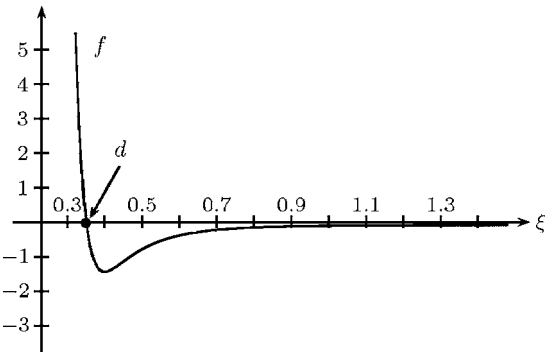

FIG. 3. van der Waals force. The units on the horizontal axis are nm and the units on the vertical axis are nN per nm^2. $d = 0.341$ nm is the unique equilibrium interlayer spacing.

In the next section, we present a straightforward analysis of the two layer bifurcation problem. Section III compares this analysis with the results of atomistic simulations of the same problem. A final concluding section summarizes our results and mentions several related problems.

II. LOCAL BIFURCATION ANALYSIS

In this section we construct bifurcation curves for the system (1). We first study the local bifurcations for the case $\varepsilon = 0$, which corresponds to axial loading with the endpoints of the layers fixed at the equilibrium spacing. To understand how the spacing effects the buckling of the layers, we then consider how solution branches perturb for $0 < \varepsilon \ll 1$, which corresponds to the layers at a slight deviation from the equilibrium spacing.

We begin with the observation that we can decouple the system (1) by introducing the variables

$$w = u_1 + u_2, \quad v = u_1 - u_2, \tag{6}$$

which yields

$$\alpha w'''' - T w'' = 0, \tag{7a}$$

$$\alpha v'''' - T v'' = 2f(v + d + \varepsilon a). \tag{7b}$$

The variables w and v satisfy boundary conditions analogous to (2).

A. Bifurcations for $\varepsilon = 0$

The local bifurcation analysis for (7a) is elementary. Seeking solutions of the form $A \sin(m\pi x/l)$, we see that nontrivial solutions are possible only at eigenvalues $T_c = T_m$, where

$$T_m := -\frac{\alpha\pi^2 m^2}{l^2} \quad \text{for } m = 1,2,\ldots . \tag{8}$$

Note that all the eigenvalues are negative, that the smallest eigenvalue in absolute value is T_1, and that the linear equation (7a) admits solutions of arbitrary amplitude A at each of its eigenvalues.

In (7b), setting $\varepsilon=0$ yields

$$\alpha v'''' - Tv'' = 2f(v+d). \tag{9}$$

We start the local bifurcation analysis of (9) by noting that $v \equiv 0$ is a solution for all T. In the usual way, we seek local descriptions of the solutions that bifurcate from this trivial branch. Hence we introduce the expansions

$$T = \tilde{T}_c + l_1\eta + l_2\frac{\eta^2}{2} + \cdots, \quad v = v_1\eta + v_2\frac{\eta^2}{2} + \cdots , \tag{10}$$

and consider the sequence of linear problems generated by substituting (10) into (9). The $\mathcal{O}(\eta)$ equation is

$$\alpha v_1'''' - \tilde{T}_c v_1'' - 2f_1 v_1 = 0, \tag{11}$$

where $f_1 := f'(d)$. Note that v_1 satisfies pinned-pinned boundary conditions like (2). Equation (11) along with the boundary conditions imply that solutions bifurcate from the trivial branch at eigenvalues $\tilde{T}_c = \tilde{T}_m$ of the form

$$\tilde{T}_m := -\frac{\alpha\pi^2 m^2}{l^2} + \frac{2f_1 l^2}{\pi^2 m^2} \quad \text{for } m = 1,2,\ldots . \tag{12}$$

As seen in Fig. 3, $f_1 < 0$ and hence $\tilde{T}_m < 0$. We let $\tilde{T}_{m_i}$ denote the ith smallest eigenvalue in absolute value, so that $0 > \tilde{T}_{m_1} > \tilde{T}_{m_2} > \cdots$.

From (11) we also discover that for $\tilde{T}_c = \tilde{T}_m$, $v_1(x) = A\phi_m(x)$, where

$$\phi_m(x) := \sqrt{2/l}\,\sin(m\pi x/l). \tag{13}$$

To choose the amplitude A of v_1, we define the parameter η in (10) as the projection of the bifurcating solution onto the normalized eigenvalue ϕ_m. Hence

$$\eta := \int_0^l v(x)\sqrt{2/l}\,\sin(m\pi x/l)dx, \tag{14}$$

which implies that $A=1$.

Taking $\tilde{T}_c = \tilde{T}_m$, we see that the $\mathcal{O}(\eta^2)$ equation for (10) is

$$\alpha v_2'''' - \tilde{T}_m v_2'' - 2f_1 v_2 = 2l_1 v_1'' + 2f_2 v_1^2, \tag{15}$$

where $f_2 := f''(d)$. To determine l_1, we apply the usual solvability condition to (15), which requires that

$$\int_0^l [2l_1 v_1'' + 2f_2 v_1^2]\phi_m(x)dx = 0. \tag{16}$$

Upon noting that

$$\int_0^l \sin^3(m\pi x/l)dx = \begin{cases} 0 & \text{for } m \text{ even}, \\ \dfrac{4l}{3m\pi} & \text{for } m \text{ odd}, \end{cases} \tag{17}$$

we solve (16) and find

$$l_1 = \begin{cases} 0 & \text{for } m \text{ even}, \\ \dfrac{16}{3\sqrt{2}}\dfrac{l^{3/2}f_2}{m^3\pi^3} & \text{for } m \text{ odd}. \end{cases} \tag{18}$$

We assume $f_2 > 0$ (see Fig. 3), so that $l_1 > 0$ if m is odd.

To summarize these computations, for m odd we have

$$\tilde{T} = \tilde{T}_m + \frac{16}{3\sqrt{2}}\frac{l^{3/2}f_2}{k^3\pi^3}\eta + \cdots , \tag{19a}$$

$$v = \phi_m\eta + \cdots , \tag{19b}$$

where $\tilde{T}_m$ is defined by (12). Note that there is a transcritical bifurcation at $\tilde{T}_m$.

B. Analysis for $\varepsilon > 0$

To study the perturbation in ε of the trivial branch of solutions for (9), we seek a solution to (7b) of the form

$$V = V_1\varepsilon + \mathcal{O}(\varepsilon^2). \tag{20}$$

Inserting (20) into (7b) yields the $\mathcal{O}(\varepsilon)$ equation

$$\alpha V_1'''' - TV_1'' - 2f_1 V_1 = 2af_1, \tag{21}$$

where V_1 satisfies boundary conditions like (2). One can check that

$$V_1 = c_1\left(\cos\zeta_1 x + \frac{1-\cos\zeta_1 l}{\sin\zeta_1 l}\sin\zeta_1 x\right) + c_3\left(\cos\zeta_2 x + \frac{1-\cos\zeta_2 l}{\sin\zeta_2 l}\sin\zeta_2 x\right) - a, \tag{22}$$

where

$$\zeta_1 := \sqrt{\frac{-T+\sqrt{T^2+8\alpha f_1}}{2\alpha}}, \quad \zeta_2 := \sqrt{\frac{-T-\sqrt{T^2+8\alpha f_1}}{2\alpha}}, \tag{23}$$

$$c_1 := a\frac{\zeta_2^2}{\zeta_2^2-\zeta_1^2}, \quad c_3 := -a\frac{\zeta_1^2}{\zeta_2^2-\zeta_1^2}. \tag{24}$$

We note that

$$\left|\frac{1-\cos\zeta l}{\sin\zeta l}\right| \to \infty \quad \text{if and only if } \zeta \to m\pi/l \text{ with } m \text{ odd}. \tag{25}$$

Also, one can check that $\zeta_j = m\pi/l$ for $j=1$ or if and only if T in (23) equals $\tilde{T}_m$ from (12). Hence V is small in amplitude unless T is near $\tilde{T}_m$ for some m.

In the next subsection, we describe how one can use (22) to construct small amplitude solutions to (1). Two such solutions are plotted in Figure 4 below.

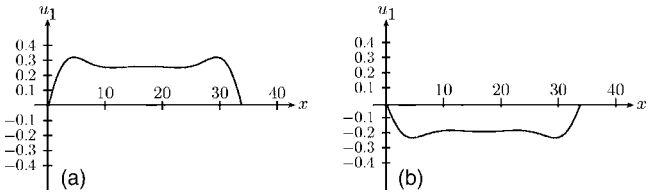

FIG. 4. Antisymmetric solutions predicted by continuum modeling. The units on both the vertical and horizontal axes are angstroms (10 Å=1 nm). The length of the layer is 3.4 nm and the compressive load is $T=-.05$ nN/nm. (a) shows the transverse displacement of only the top layer u_1 to $\mathcal{O}(\varepsilon)$ when $a=-1$ nm and $\varepsilon=0.03$, which corresponds to the two layers spaced approximately 0.3 Å less than the equilibrium spacing of 3.41 Å. (b) shows the transverse displacement of the top layer u_1 to $\mathcal{O}(\varepsilon)$ when $a=1$ nm and $\varepsilon=0.02$, which corresponds to the two layers spaced approximately 0.2 Å greater than the equilibrium spacing. Cf. Figs. 7 and 10 below.

C. Bifurcation diagrams

In this subsection we construct bifurcation diagrams for the system (1). Recall that T_1 is the first eigenvalue for (7a) and that $\tilde{T}_{m_1}$ is the first eigenvalue for (9). Equations (8) and (12) imply that $\tilde{T}_{m_1}<T_1$.

Before constructing the bifurcation diagrams, we note that (6) implies that

$$u_1=\frac{w+v}{2},\quad u_2=\frac{w-v}{2}. \tag{26}$$

Hence if $w=0$, then $u_1=v/2$ and $u_2=-v/2=-u_1$. In particular for $T_1\ll T<0$, where T_1 is given by (8), and for $0<\varepsilon\ll 1$, the solution to (1) is antisymmetric, small in amplitude, and $u_1=\varepsilon V_1+\mathcal{O}(\varepsilon^2)$, where V_1 is defined by (22). Two examples of such antisymmetric solutions are plotted in Fig. 4. To plot these solutions, we assume that $\alpha=0.2$ nN nm, a value consistent with those commonly used in the literature,[30,31,4] and $f_1=-84.08$ nN/nm^3 [see (5), (4) and recall that $f_1:=f'(d)$].

Also from (26), it is clear that if $|w|$ is large and $|v|$ is small, u_1 is approximately equal to u_2. Therefore, a solution w to (7a) with large amplitude corresponds to a symmetric deformation of the two layers.

The expansions constructed in the previous two subsections imply that solutions to (7) can be represented by the bifurcation curves in Fig. 5. To construct Fig. 5, we have

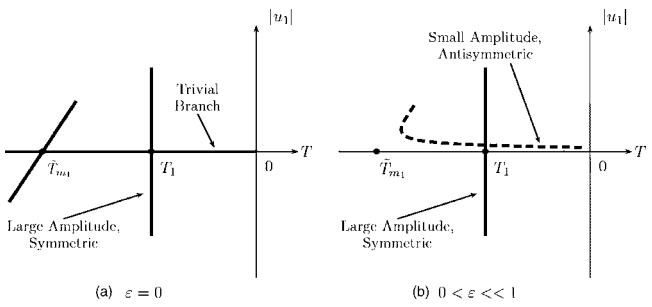

FIG. 5. Bifurcation diagrams.

assumed that $\tilde{T}_{m_1}>T_2$.

Figure 5(a) shows the bifurcation diagram for $\varepsilon=0$. The vertical axis is the amplitude of u_1. The labeling of the relevant branches indicates the corresponding amplitude of u_2. From the figure we see that the trivial branch $u_1=u_2=0$ bifurcates to large amplitude symmetric solutions at $T=T_1$. We suspect that a linear stability analysis would show that the trivial branch loses stability at T_1 and that hence the antisymmetric bifurcation at $T=\tilde{T}_{m_1}$ is never observed. This conclusion is supported by the simulation results presented in the next section. When $0<\varepsilon\ll 1$, Fig. 5(b) shows that the trivial branch $u_1=u_2=0$ perturbs to a small-amplitude antisymmetric solution, as indicated by (20) and (22). However, as T approaches T_1, this small-amplitude antisymmetric solution bifurcates to a large amplitude symmetric solution. In the next section we compare these qualitative observations, which are based on continuum modeling, with the buckling patterns predicted from atomistic simulations.

Note that we have assumed in constructing Fig. 5 that m_1 is odd. If m_1 were even, the transcritical bifurcation at $\tilde{T}_{m_1}$ in Fig. 5(a) would instead be a pitchfork bifurcation. How the bifurcation at $\tilde{T}_{m_1}$ breaks because of small deviations from the equilibrium spacing is studied in detail via imperfect bifurcation techniques in Ref. 32.

III. ATOMISTIC SIMULATIONS

In this section, we present the results from atomistic simulations of interacting graphene layers subject to compressive edge loading. These results agree qualitatively with the analysis of the previous section based on continuum modeling.

We discuss results from three simulations. In each of these, two parallel graphene layers are spaced D angstroms apart, with $D=3.1$ Å in the first simulation, $D=3.41$ Å in the second simulation, and $D=3.6$ Å in third simulation. To create the atomic model of the stacked graphene layers, an ideal graphite structure corresponding to ABAB$\cdots$ stacking was used. The width of the bottom layer, i.e., the distance between the pair of opposite edges subject to compressive loading, is 34.08 Å in all three simulations. Because of how the layers are stacked, the corresponding width of the top layer is 32.7 Å in all three simulations. Along the other pair of opposite edges the boundary conditions are periodic and each layer can be viewed as infinite in this direction. See Figs. 1 and 6.

Figure 6 shows the top graphene layer from the simulations. In each simulation, the positions of narrow strips of atoms at the left and right edges of each layer were prescribed. The two strips at the left edges of the layers were kept fixed. To simulate compressive edge loading, the two strips at the right edges were incrementally moved toward the left while being kept parallel to each other and the fixed distance D apart. All the other atoms in both layers were free to relax. The atoms in the edge strips on the right were each moved leftward in 0.001 Å increments, after which the free atoms between the strips were relaxed using a code based on the molecular dynamics (MD) code by Brenner. Annealing

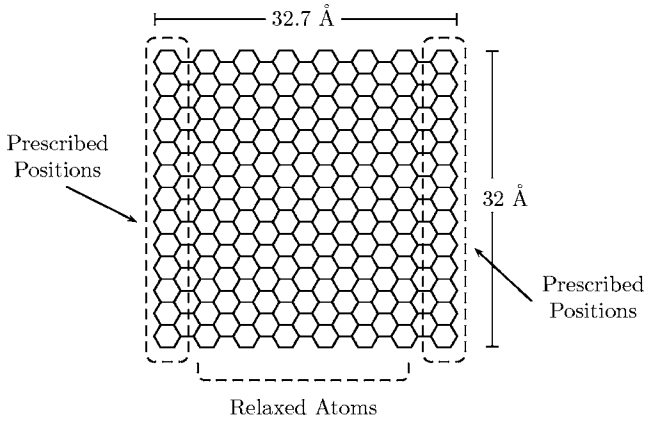

FIG. 6. Top view of the top graphene layer. The positions of atoms on the left and right edges of each layer are prescribed during the simulation. Atoms in the middle are free to relax after each displacement of the right edge.

and quenching simulations were performed using the MD technique with the Nordsieck predictor-corrector integration algorithm. However, vibrational relaxations were present at even very low temperatures (1×10^{-4} K). Thus, the simulations were continued with only energy minimization calculations. The minimization routines were based on steepest descent algorithms and conjugate gradient algorithms. (For our structures, the best minimization was obtained using the steepest descent algorithm.)

In our calculations, the Tersoff-Brenner empirical potential energy function[33] was used to model the interactions between bonded atoms within each layer. This potential, which reproduces lattice constants, binding energies, elastic constants, etc. of graphite and diamond very well, is widely used to explore the properties of graphite and the fullerenes. See Refs. 34 and 4 and the references therein.

Because a fundamental input into any atomistic simulation is the definition of the interatomic potential, we note

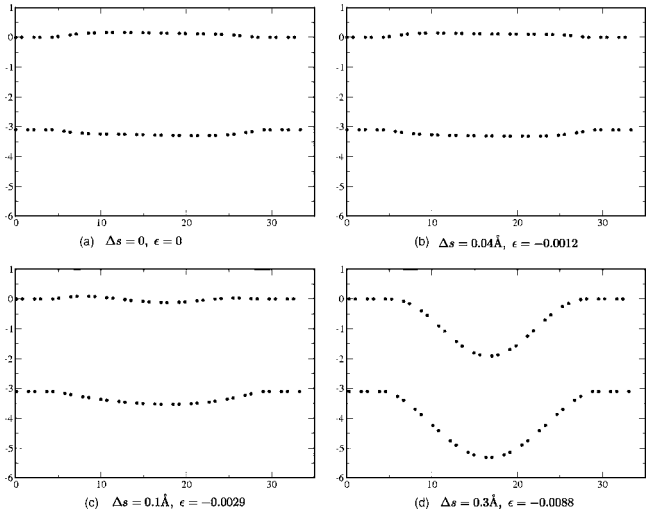

FIG. 7. Atomistic simulation, $D=3.10$ Å. Δs is the displacement of the edge strips. $\epsilon:=-\Delta s/34$ is the compressive strain, where 34 Å is the length of the bottom layer. The units on both the vertical and horizontal axes are angstroms. See also Fig. 8(a).

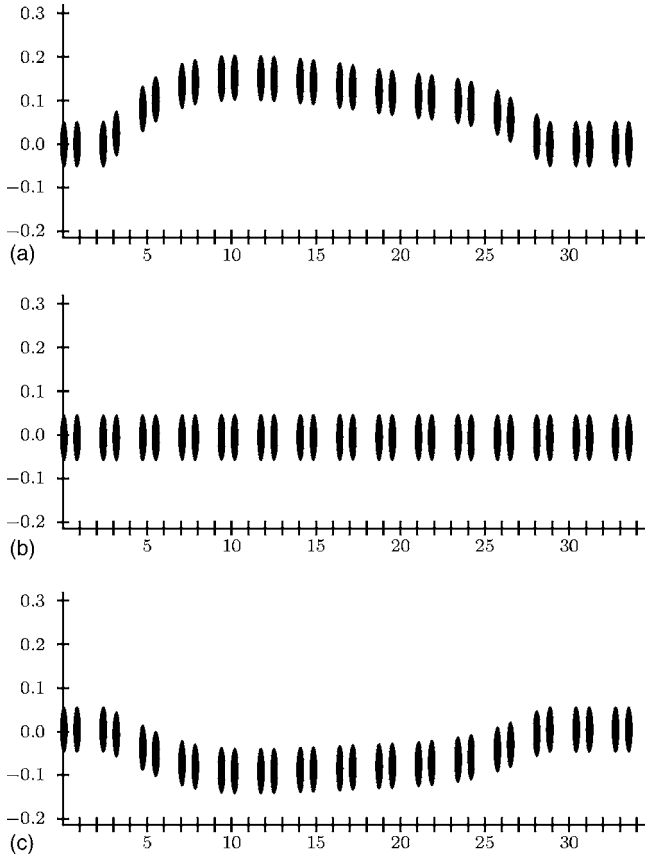

FIG. 8. Displacements prior to edge compression. Figure (a) above is the same as part of Fig. 7(a) but rescaled to show more clearly the shape of the top layer. Likewise, (b) above is a rescaling of part of Fig. 9(a), and (c) above is a rescaling of part of Fig. 10(a). The units on both the vertical and horizontal axes are angstroms.

several other possibilities for carbon nanotube or graphene systems. These include first-principles electronic structure methods based on density functional theory (DFT),[35] quantum-based interatomic potentials based on tight-binding (TB) representations of electronic structure,[36] hybrid ReaxFF-Tersoff models,[37] and methods based on harmonic-type potentials.[29] Choosing a particular method entails a trade-off between accuracy and computational effort. (See Ref. 38 for an overview of this trade-off.) We use the Tersoff-Brenner potential because, computationally, it is relatively less costly and because it is widely accepted as producing accurate results for equilibrium or near-equilibrium situations.

For our calculations, we use also Girifalco's Lennard-Jones potential V, defined immediately following (3) with the same constants as given in (4), to model the interlayer van der Waals interactions. The cutoff radius for the potential was approximately 8.5 Å.

Results from the first simulation, with $D=3.1$ Å, are depicted in Fig. 7. Note that the figure shows a side view of the layers, so that each dot on a layer represents several carbon atoms that align across the width of the layer. Fig. 7(a) shows the layers after they were relaxed from their initial parallel configuration but before the edges were moved. Figure 8(a) shows a part of Fig. 7(a) rescaled so that one can see more

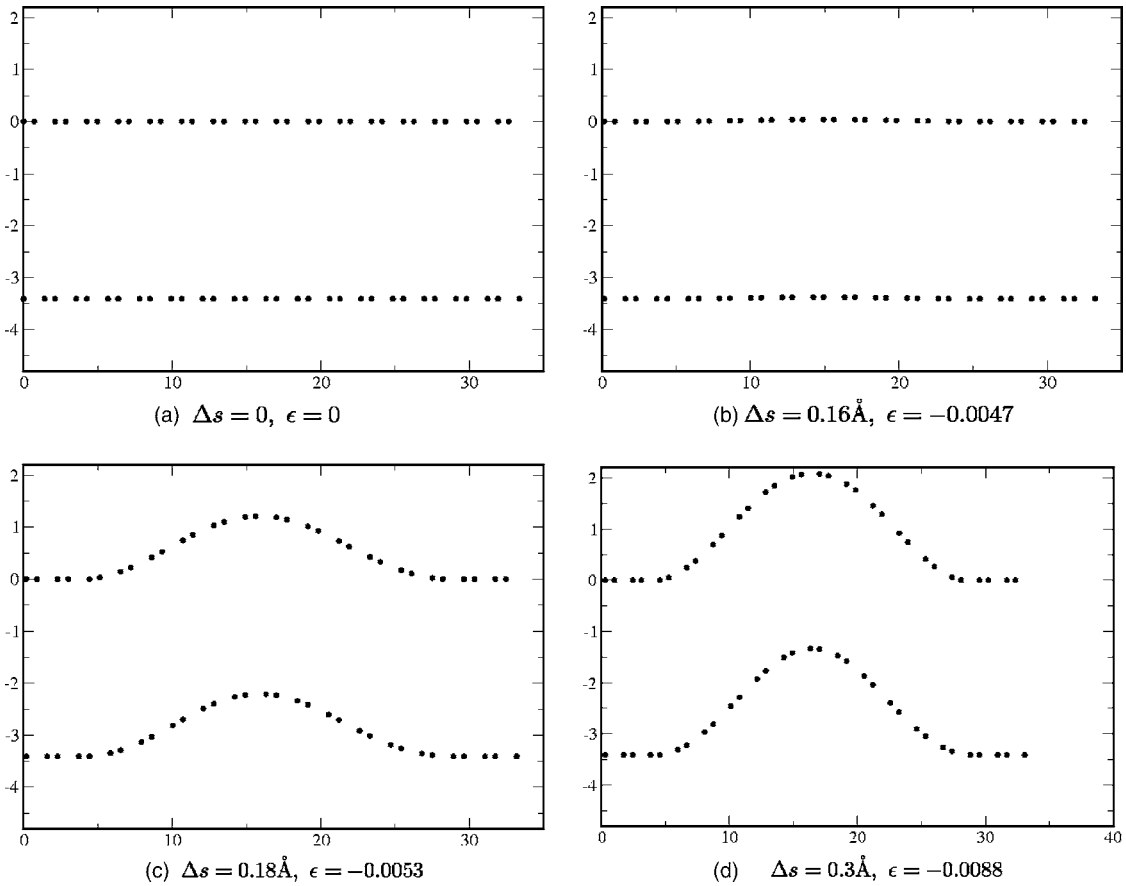

FIG. 9. Atomistic simulation, $D=3.41$ Å. Δs is the displacement of the edge strips. $\epsilon := -\Delta s/34$ is the compressive strain, where 34 Å is the length of each layer. The units on both the vertical and horizontal axes are angstroms.

clearly the shape of the transverse displacement prior to compression. Figures 7(b)–7(d) correspond to edge compressions of 0.04 Å, 0.1 Å, and 0.3 Å. In Figs. 7(a) and 7(b), we see a small-amplitude, antisymmetric deformation. Note that the two layers bow outward, as one would expect because the spacing is less than the equilibrium spacing and hence the van der Waals force between the layers is repulsive. Figure 7(c) shows the onset of a large-amplitude symmetric bifurcation, while Fig. 7(d) shows the symmetrically buckled layers. This sequence of deformations is consistent with the predictions of Fig. 5(b). Also, a comparison of Figs. 7(a) and 7(b) [see also Fig. 8(a)] and 4(a) shows that for small compressive loads the continuum and atomistic approaches agree on the qualitative shape of the antisymmetric deformation of the layers.

The second simulation, in which the interlayer spacing is 3.41 Å, is depicted in Fig. 9. Figure 9(a) shows the layers after they have relaxed from their initial parallel configuration but before the edges were moved. Figure 8(b) shows a part of Fig. 9(a) rescaled so that one can see more clearly the shape of the transverse displacement prior to compression. Figures 9(b)–9(d) correspond to edge compressions of 0.16 Å, 0.18 Å, and 0.3 Å. In Figs. 9(a) and 9(b), we see essentially no transverse displacement of the layers, as one would expect because the layers are at their equilibrium spacing. Figure 9(c) shows the onset of a large-amplitude symmetric bifurcation, while Fig. 9(d) shows the symmetrically buckled layers. This sequence of deformations is consistent with the predictions of the continuum model for $\varepsilon = 0$; see Fig. 5(a).

The interlayer spacing was 3.6 Å for the final simulation. Figure 10(a) shows the layers after they have relaxed from their initial parallel configuration but before the edges were compressed. Figure 8(c) shows a part of Fig. 10(a) rescaled so that one can see more clearly the shape of the transverse displacement prior to compression. Figures 10(b)–10(d) correspond to edge compressions of 0.05 Å, 0.1 Å, and 0.3 Å. In Fig. 10(a) and 10(b), we see a small-amplitude, antisymmetric deformation in which the two layers are bowed inward, as one would expect because the interlayer spacing is greater than the equilibrium spacing and hence the van der Waals force between the layers is attractive. As in the previous two simulations, we see in Fig. 10(c) the onset of a large-amplitude symmetric bifurcation, while in Fig. 10(d) we see the symmetrically buckled layers. Again, we note that Figs. 10(a) and 10(b) [see also Fig. 8(a)] and 4(b) show good agreement on the shape of the transverse displacement of the layers.

For any comparison of the atomistic and continuum results, it is important to note the mismatch between the apparent boundary conditions in the atomistic simulations and those used in the continuum problem. As described in Sec. I, classical hinged-hinged boundary conditions are enforced in the continuum problem. See (2). We use these boundary con-

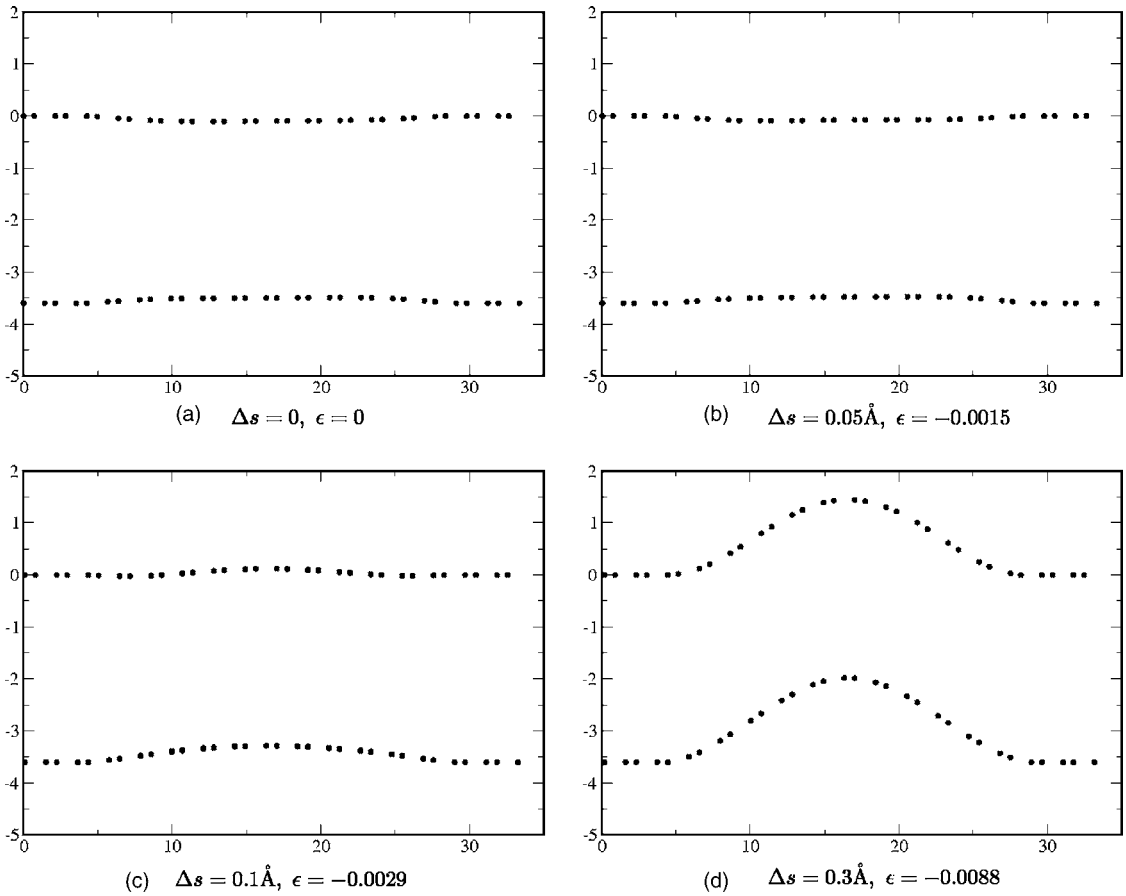

FIG. 10. Atomistic simulation, $D=3.60$ Å. Δs is the displacement of the edge strips. $\epsilon := -\Delta s/34$ is the compressive strain, where 34 Å is the length of each layer. The units on both the vertical and horizontal axes are angstroms.

ditions because they are perhaps the most familiar for Euler-Bernoulli beam buckling and lead to the simplest expressions in our series expansions for solutions.

Describing the boundary conditions in the atomistic simulation is more subtle. As noted above, during the simulation the positions of several rows of atoms at the left and right edges of each layer is prescribed. See Fig. 6. To determine the boundary conditions, one perhaps should ignore these prescribed atoms. Hence one could place the boundary at the interior most rows of prescribed atoms, i.e., the fourth dot in from the left and the fourth dot in from the right for each of the layers depicted in Figs. 7–10. The transverse displacement at these points is zero. However, numerical approximation of the data from the simulations shows that the second derivative of the transverse displacement is nonzero at the end points. We believe that this discrepancy explains in part the difference between the deformed shapes of the layers predicted by the continuum model and the atomistic simulation.

In this paper, where we focus on qualitatively comparing the continuum and atomistic approaches, we do not consider different boundary conditions for the beam equation. Doing so would not change the qualitative buckling pattern predicted by the continuum model. On the other hand, we are currently exploring quantitative comparisons of the continuum model and atomistic simulations.[39] For this, we numerically solve the beam equation with zero transverse displacements and a nonzero bending moments M at the boundaries. We then fit numerically the bending stiffness α and the moment M by minimizing the differences between the displacements predicted by the atomistic simulation and those predicted by the numerical solution of the boundary value problem. For the values of M and α determined by this minimization, we obtain excellent agreement between the deflected shapes predicted by the continuum and atomistic approaches.

Figure 11 presents an energy analysis of the second atomistic simulation, for which $D=3.41$ Å. The drop in energy at about 0.18 Å corresponds to the start of the buckling observed in Figs. 9(c) and 9(d). The corresponding drop in energy for the first and third simulations is difficult to discern and we do not present the corresponding graphs.

We close this section with a remark on the buckling loads in each of the three simulations. As depicted in Fig. 7(c), in the first simulation the symmetric buckling begins at an edge displacement Δs of about 0.1 Å. Using data from the simulation, one can compute that the total compressive force on, say, the left edge of the top layer for $\Delta s=0.1$ Å is approximately 0.09 nN/nm. For the other two simulations, one can likewise compute that the compressive loads at the start of the buckling [Figs. 9(c) and 10(c)] are approximately 0.17 nN/nm and 0.09 nN/nm. Now recall that the continuum analysis predicts that the symmetric buckling occurs at the critical load T_1, which is given by (8) with $m=1$.

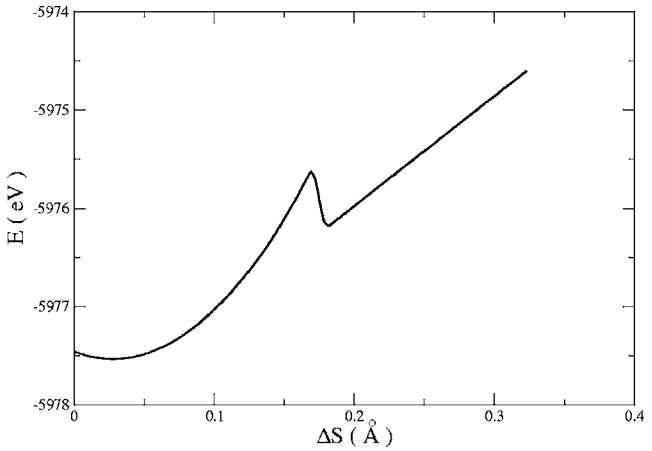

FIG. 11. Energy analysis. This figure shows the total energy of the two layer system as a function of the displacement of the edge strips for the simulation depicted in Fig. 9.

Taking $\alpha=0.2$ nN nm and $l=3.4$ nm yields $T_1=-0.1708$ nN/nm. This value agrees well with the buckling load observed in the second simulation, in which the interlayer spacing corresponds to the equilibrium spacing. However for the other two simulations, in which the interlayer deviates slightly from the equilibrium, the continuum analysis fails to accurately predict the symmetric buckling load. One possible explanation is that the bending stiffness α depends on the interlayer spacing; as noted above, part of our current research explores this question.

IV. CONCLUSION

In this paper we consider two parallel graphene layers that interact by a nonlinear van der Waals force. To study the buckling of these interacting layers under compressive edge loading, we carry out both a bifurcation analysis based on continuum mechanical modeling as well as atomistic simulations. The continuum description is motivated by a multishell model of multiwalled nanotubes proposed in Ref. 8.

Our basic conclusion is that the sequence of deformations observed in the atomistic simulations matches qualitatively the bifurcation diagram constructed by an analysis of the continuum model. Specifically, both the continuum and atomistic approaches predict the following. When the initial spacing between the layers is slightly less than the equilibrium spacing predicted by the van der Waals force, the layers exhibit small amplitude, antisymmetric deformations for small compressive edge loads. Both the continuum and atomistic results predict that these antisymmetric deformations are bowed outward. See Figs. 4(a), 7(a), and 7(b). The antisymmetric solutions buckle to large amplitude symmetric deformations as the compressive force approaches some critical load. See Figs. 5(b), 7(c), and 7(d). On the other hand, when the initial spacing between the layers equals the equilibrium spacing predicted by the van der Waals force, both continuum and atomistic approaches predict no deformation up to the critical load, at which the trivial solution bifurcates to large amplitude symmetric deformations. See Figs. 5(a) and 9(a)–9(d). The case in which the initial spacing between the layers is slightly greater than the equilibrium spacing predicted by the van der Waals force is analogous to the slightly-less-than-equilibrium case, except that the small amplitude antisymmetric deformations bow inward. See Figs. 4(b), 10(a), and 10(b). The agreement between the continuum model and the atomistic simulations provides some verification of the multishell model for carbon nanotubes.

In Ref. 32 we study an interesting variation on the problem considered here. Namely, we consider a pair of interacting graphene layers where only one layer can deform. The other layer is required to remain flat. In this case the equilibrium equation for the deformable layer is essentially the same as (7b) and hence the buckling is described by the antisymmetric branch in the bifurcation diagram in Fig. 5. Using the mathematical tools of imperfect bifurcation theory, we make a careful study of this bifurcation problem, and we compare these results to the predictions of atomistic simulations.

We close by noting that the strong qualitative agreement between the continuum modeling and the atomistic simulations of this problem suggests more careful, quantitative comparisons. Part of our current research[39] includes numerical work to compare the exact shape of deformations and the buckling loads predicted by continuum and atomistic approaches. This work is described briefly in the discussion of boundary conditions in the previous section. Here we note that to further test the validity of continuum models, our quantitative comparisons[39] include a study of how the predicted stiffness of the layer depends on the interlayer spacing.

*Corresponding author.
Electronic address: pwilber@math.uakron.edu

[1] R. S. Ruoff and D. C. Lorents, Carbon **33**, 925 (1995).
[2] J.-P. Salvetat, J.-M. Bonard, N. H. Thomson, A. J. Kulik, L. Forró, W. Benoit, and L. Zuppiroli, Appl. Phys. A: Mater. Sci. Process. **69**, 255 (1999).
[3] M.-F. Yu, J. Eng. Mater. Technol. **126**, 271 (2004).
[4] B. I. Yakobson, C. J. Brabec, and J. Bernholc, Phys. Rev. Lett. **76**, 2511 (1996).
[5] M. J. Buehler, Y. Kong, and H. Gao, J. Eng. Mater. Technol. **126**, 245 (2004).
[6] O. Lourie, D. M. Cox, and H. D. Wagner, Phys. Rev. Lett. **81**, 1638 (1998).
[7] M. J. Buehler, Y. Kong, H. Gao, and Y. Huang, J. Eng. Mater. Technol. **128**, 3 (2006).
[8] C. Q. Ru, J. Appl. Phys. **87**, 7227 (2000).
[9] C. Q. Ru, J. Mech. Phys. Solids **49**, 1265 (2001).
[10] C. Q. Ru, J. Appl. Phys. **89**, 3426 (2001).
[11] C. Y. Wang, C. Q. Ru, and A. Mioduchowski, Int. J. Solids Struct. **40**, 3893 (2003).

[12] C. Y. Wang, C. Q. Ru, and A. Mioduchowski, J. Nanosci. Nanotechnol. **3**, 199 (2003).
[13] C. Q. Ru, Phys. Rev. B **62**, 16962 (2000).
[14] Q. Han and G. Lu, Eur. J. Mech. A/Solids **22**, 875 (2003).
[15] Hui-Shen Shen, Int. J. Solids Struct. **41**, 2643 (2004).
[16] X. Q. He, S. Kitipornchai, and K. M. Liew, J. Mech. Phys. Solids **53**(2), 303 (2005).
[17] S. Kitipornchai, X. Q. He, and K. M. Liew, J. Appl. Phys. **97**, 114318 (2005).
[18] G. Cao and X. Chen, Phys. Rev. B **73**, 155435 (2006).
[19] A. Sears and R. C. Batra, Phys. Rev. B **73**, 085410 (2006).
[20] M. Nishio, S. Akita, and Y. Nakayama, Jpn. J. Appl. Phys., Part 2 **44**, L1097 (2005).
[21] A. M. Affoune, B. L. V. Prasad, H. Sato, T. Enoki, Y. Kaburagi, and Y. Hishiyama, Chem. Phys. Lett. **248**(1–2), 17 (2001).
[22] S. Horiuchi, T. Gotou, M. Fujiwara, T. Asaka, T. Yokosawa, and Y. Matsui, Appl. Phys. Lett. **84**, 2403 (2004).
[23] K. S. Novoselov, D. Jiang, F. Schedin, T. J. Booth, V. V. Khotkevich, S. V. Morozov, and A. K. Geim, Proc. Natl. Acad. Sci. U.S.A. **102**, 10451 (2005).
[24] H. C. Schniepp, J.-L. Li, M. J. McAllister, H. Sai, M. Herrera-Alonso, D. H. Adamson, R. K. Prud'homme, R. Car, D. A. Saville, and I. A. Aksay, J. Phys. Chem. B **110**, 8535 (2006).
[25] I. Cabria, J. A. Alonso, and M. J. Lopez, Phys. Status Solidi A **203**, 1105 (2006).
[26] S. Kitipornchai, X. Q. He, and K. M. Liew, Phys. Rev. B **72**, 075443 (2005).
[27] L. A. Girifalco, M. Hodak, and R. S. Lee, Phys. Rev. B **62**, 13104 (2000).
[28] L. A. Girifalco and R. A. Lad, J. Chem. Phys. **25**, 693 (1956).
[29] J. Zou, B. Ji, X. Feng, and H. Gao, Nano Lett. **6**(3), 430 (2006).
[30] D. H. Robertson, D. W. Brenner, and J. W. Mintmire, Phys. Rev. B **45**, 12592 (1992).
[31] C. Q. Ru, Phys. Rev. B **62**, 9973 (2000).
[32] J. P. Wilber, A. Buldum, C. B. Clemons, D. D. Quinn, and G. W. Young (unpublished).
[33] D. W. Brenner, Phys. Rev. B **42**, 9458 (1990).
[34] A. Buldum, *Modelling and simulations of carbon nanotubes*, edited by P. B. Balbuena and J. M. Seminario, in Nanomaterials: Design and Simulation (Elsevier, 2006).
[35] A. Maiti, Chem. Phys. Lett. **331**, 21 (2000).
[36] B. Liu, H. Jiang, H. T. Johnson, and Y. Huang, J. Mech. Phys. Solids **52**(1), 1 (2004).
[37] R. King and M. J. Buehler, *Atomistic modeling of elasticity and fracture of a (10,10) single wall carbon nanotube*, MRS Proc. No. 924E (2006).
[38] M. J. Buehler, Lecture notes for "From nano to macro: Introduction to atomistic modeling techniques," Lecture 1. Department of Civil and Environmental Engineering, MIT. Available online at http://web.mit.edu/mbuehler/www/Teaching/IAP2006/intro.htm
[39] M. W. Roberts, A. Buldum, C. B. Clemons, D. D. Quinn, J. P. Wilber, and G. W. Young (unpublished).